Geophys. J. Int. (2009) doi: 10.1111/j.1365-246X.2008.04029.x

Coupled afterslip and viscoelastic flow following the 2002 Denali Fault, Alaska earthquake

Kaj M. Johnson,[1] Roland Bürgmann[2] and Jeffrey T. Freymueller[3]

[1]*Department of Geological Sciences, Indiana University, IN, USA. E-mail: kajjohns@indiana.edu*
[2]*Department of Earth and Planetary Science, University of California, Berkeley, CA, USA*
[3]*Department of Geology and Geophysics, University of Alaska, Fairbanks, AK, USA*

Accepted 2008 November 4. Received 2008 November 4; in original form 2008 May 20

SUMMARY

Models of postseismic deformation following the 2002 *M* 7.9 Denali Fault, Alaska earthquake provide insight into the rheologic structure of the Alaskan lithosphere and the physical processes activated following a large earthquake. We model coseismic GPS displacements and 4 yr of postseismic GPS position time-series with a coupled model of afterslip on the fault in the lithosphere and distributed viscous flow in the asthenosphere. Afterslip is assumed to be governed by a simplified version of a laboratory-derived rate-strengthening friction law that is characterized with a single parameter, $\sigma(a - b)$, where σ is the effective normal stress on the fault and $a - b$ is a dimensionless empirical parameter. Afterslip is driven by coseismic stress changes on the fault generated by the main shock. The lithosphere is modelled as an elastic plate overlying a linear, Maxwell, viscoelastic asthenosphere. We devise a scheme to simultaneously estimate the distributions of coseismic slip and afterslip, friction parameters, lithosphere thickness and asthenosphere viscosity. The postseismic GPS time-series are best reproduced with a 45–85 km thick elastic lithosphere overlying an asthenosphere of viscosity 0.6–1.5 $\times$ 10^{19} Pa s. The 45–85 km elastic lithosphere thickness is greater than or equal to the average crustal thickness in the region suggesting that distributed postseismic flow occurs largely within the mantle while postseismic deformation in the crust is confined largely to slip on a discrete fault penetrating the entire crust and perhaps into the uppermost mantle. For typical laboratory values of $a - b$ of order 10^{-2} at temperatures corresponding to the inferred depth of afterslip, the estimated effective normal stress on the fault is $\sim$50 MPa, which is about an order of magnitude lower than effective normal stresses at hydrostatic pore pressure. Previous studies showed that models with linear Newtonian rheology cannot reproduce the observed GPS time-series but that models incorporating non-linear or biviscous flow of the mantle do fit the data. We show that a model with afterslip governed by a non-linear fault zone rheology coupled to Newtonian mantle flow is sufficient to reproduce the GPS time-series.

Key words: Satellite geodesy; Transient deformation; Friction; Dynamics and mechanics of faulting; Rheology: crust and lithosphere; Rheology and friction of fault zones.

1 INTRODUCTION

Measurements of transient deformation following earthquakes can be used to probe the rheologic structure of the lithosphere. GPS measurements of the temporal evolution of positions of points on the surface of the Earth have been utilized to identify multiple deformation processes following earthquakes including viscous flow in the lower crust and/or upper mantle, afterslip at crustal depths on the fault, and poroelastic response to fluid flow in the crust (see Bürgmann & Dresen 2008, for a review). The 2002 Denali Fault, Alaska earthquake and 4 yr of continued postseismic deformation were well recorded with campaign and continuous GPS data (e.g. Freed *et al.* 2006b) that allow us to infer rheologic properties of the central and southern Alaskan lithosphere. The Denali earthquake ruptured three fault segments shown in Fig. 1 including the Susitna Glacier thrust and the Denali and Totschunda right-lateral strike–slip faults. The Denali Fault is a large active intraplate fault that accommodates westward rotation of the crustal block bounded by the Aleutian megathrust to the south and the Denali Fault to the north.

Previous studies demonstrate that at least two deformation mechanisms are needed to explain the Denali postseismic GPS data and that flow in the mantle below at least 40 km depth contributes significantly to the observed postseismic surface deformation. Pollitz (2005) showed that the GPS time-series positions for the first 1.5 yr following the earthquake are consistent with viscous flow below an elastic upper crust assuming a two-component biviscous rheology (Burgers body) for the mantle characterized by steady-state

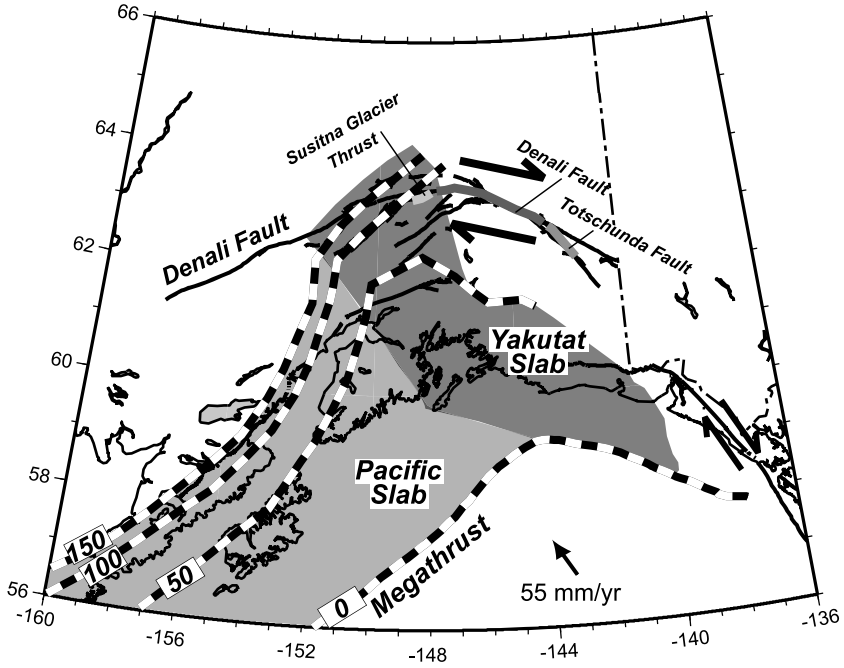

Figure 1. Tectonic setting after Eberhart-Phillips *et al.* (2006) showing inferred extent of Pacific and Yakutat slab and depth contours of the plate interface. The Denali Fault earthquake ruptured the Susitna Glacier thrust and sections of the Denali and Totschunda Faults.

viscosity of 2.8×10^{18} Pa s and a transient viscosity of 1.0×10^{17} Pa s. Pollitz (2005) modelled the lower crust as a single-component (Maxwell) viscous layer between 15 and 40 km depth with viscosity of order 10^{19} Pa s. Freed *et al.* (2006a) showed that significant postseismic flow below a depth of about 60 km is required to explain the displacements of GPS sites located far from the fault. Freed *et al.* (2006b) showed that the GPS time-series data cannot be explained with flow of a Newtonian viscous mantle but can be explained by flow of a mantle with non-linear, power-law dependence of strain rate on stress. Freed *et al.* (2006a) showed that the GPS data and models cannot distinguish between distributed lower crustal flow (between 30 and 60 km depth) and localized afterslip on the fault, but it is clear from Freed *et al.* (2006b) that shallow afterslip (less than 30 km depth) on the fault is required to fit the displacements at sites nearest the fault. The main conclusions from these studies regarding the rheology of the Alaskan lithosphere include: (1) flow in the mantle below at least 40 km depth is required to explain the motions of sites located far from the fault (>100 km); (2) a shallower source (likely afterslip) in the crust is necessary to explain motions of sites near the fault; (3) it is not possible to reproduce the observed GPS time-series either near or far from the fault with models consisting of strictly Newtonian rheology (mantle flow and/or flow within a crustal viscous shear zone) and (4) the GPS time-series at sites far from the fault can be reproduced with models consisting of flow in a non-linear, power-law viscous mantle or a linear biviscous body.

None of the above studies attempt to match GPS time-series data with models that incorporate the coupled processes of afterslip and distributed viscous flow. Here, we investigate the relative contributions of afterslip on the fault and viscous flow in the mantle to the observed GPS time-series for 4 yr following the 2002 Denali earthquake. We model postseismic deformation with afterslip on a fault in an elastic upper crust coupled to distributed flow in a linear Maxwell viscoelastic lower crust and/or upper mantle. The afterslip is governed by a rate-strengthening friction law. We show that, as suggested by Freed *et al.* (2006a), combined mechanisms of afterslip and deep viscous flow are needed to explain the GPS data. We also show that a non-linear viscous or biviscous rheology for the mantle is not required by the data; flow of a linear Maxwell viscous mantle coupled to rate-strengthening afterslip is sufficient to explain the observations.

2 DATA

The GPS time-series used here span the time from the day after the earthquake (2002 November 4) through the end of 2007 March, approximately 4.5 yr after the earthquake. Each day of GPS data from sites in Alaska and the surrounding area was analysed using the GIPSY-OASIS version 4 software and the JPL non-fiducial orbits. Details of the data analysis are given in Freymueller *et al.* (2008). Each daily solution is then transformed into the ITRF2000 reference frame (IGb00 realization) using roughly 20 sites distributed across about 25 per cent of the surface of the Earth. This results in time-series of station positions in ITRF2000.

Because we are interested primarily in modelling the transient behaviour following the earthquake, we modified the post-earthquake time-series by subtracting the pre-earthquake velocity of the site from the post-earthquake time-series, giving a time-series that should reflect only the transient deformation. We used the pre-earthquake velocities of Freymueller *et al.* (2008) for sites that were measured before and after the earthquake. In some cases, we have extensive post-earthquake observations from sites that had no pre-earthquake data, or only limited pre-earthquake data. In such cases, we used either the pre-earthquake velocity of a nearby site, or interpolated between sites, or used the estimated velocity based on a tectonic model. The model used for this is an updated version of the model presented in Fletcher (2002). We only used time-series from sites where we could determine a pre-earthquake velocity with an estimated precision of better than 3–4 mm yr^{-1}. Because the

postseismic deformation for most sites is an order of magnitude more rapid, this represents only a small error in the time-series data.

The main advantage of this approach is that it frees us from having to model the complex deformation of much of southern Alaska. The pre-earthquake velocities in southern Alaska result from the superposition of several separate deformation sources (Freymueller *et al.* 2008), and by removing the pre-earthquake velocities we need only to model what has changed as a result of the earthquake. We make the assumption here that all of the pre-earthquake deformation sources do not change with time, except for the afterslip and viscoelastic relaxation model described in the next section. We later relax that assumption by estimating an additional component in the model due to changes in the slip deficit distribution on the subducting plate interface.

3 MODEL AND INVERSION

3.1 Afterslip model

We idealize the Alaskan lithosphere and asthenosphere with a homogeneous elastic plate overlying a Maxwell viscoelastic half-space with uniform viscosity, η, and shear modulus, μ (uniform relaxation time, $t_R = 2\eta/\mu$) as illustrated in Fig. 2. The fault cuts through the entire elastic plate but does not penetrate into the viscoelastic substrate. The fault is discretized into 5.5 × 1.5 km rectangular patches. For now, we ignore the complexities introduced by the presence of the subducting slab and lateral variations in crustal properties, but in the discussion we address the possible influences of these lateral variations on our results.

For simplicity, we only consider the strike–slip component of fault slip. To induce coupled afterslip and viscoelastic flow, we impose coseismic slip on fault patches above 18 km depth. The stresses on the fault and within the viscoelastic substrate induced by coseismic slip are then relaxed by localized afterslip on the fault and distributed viscous flow at depth. We assume that afterslip is governed by a rate-strengthening friction law that relates the strike-parallel shear stress, τ, and normal stress, σ, on the fault to the strike-parallel component of slip rate, v,

$$\tau = \sigma \{\mu + (a - b) \ln(v/v^*)\}, \tag{1}$$

where μ is the nominal coefficient of friction, v^* is a reference sliding velocity and $a - b$ is a dimensionless friction parameter that is found in lab experiments to be typically of order 10^{-3} to 10^{-2}. This formulation is a simplified version of a more general rate-and-state-dependent frictional behaviour inferred from laboratory experiments (e.g. Dieterich 1981) that has also been adopted by a number of previous afterslip studies (e.g. Marone *et al.* 1991; Linker & Rice 1997; Hearn *et al.* 2002; Perfettini & Avouac 2007a).

We need the stress on a patch at any time to compute the slip rate using eq. (1). Let $\mathbf{g}_i(t - t_0)$ be a $1 \times m$ vector of Green's functions that relates the shear stress, τ_i, on the ith patch at time t to unit slip on m patches at time t_0. The g_i are time-dependent because viscous flow in the asthenosphere varies with time. The $\mathbf{g}_i$ are computed using semi-analytical propagator matrix methods (e.g. Fukahata & Matsu'ura 2006). Let $\tau_i^c(t)$ be the shear stress induced on the ith patch by coseismic slip and associated viscous flow. Then, the stress on the ith patch at time t, due to coseismic slip and postseismic slip-rate history $\mathbf{v}(t)$, where $\mathbf{v}(t)$ is a $m \times 1$ vector of slip rates, is

$$\tau_i(t) = \tau_i^c(t) + \int_0^t \mathbf{g}_i(t - t')\mathbf{v}(t')\,\mathrm{d}t'. \tag{2}$$

We approximate the integral by discretizing time into N discrete steps with duration $\delta_1, \delta_2, \ldots, \delta_N$ where N and δ_k will be determined in the integration scheme. Stress and slip rate is computed at the midpoint of time increments. The midpoint of the jth time increment is $t_j = 0.5\delta_j + \sum_{k=1}^{j-1} \delta_k$. Then, the stress on the ith patch during the

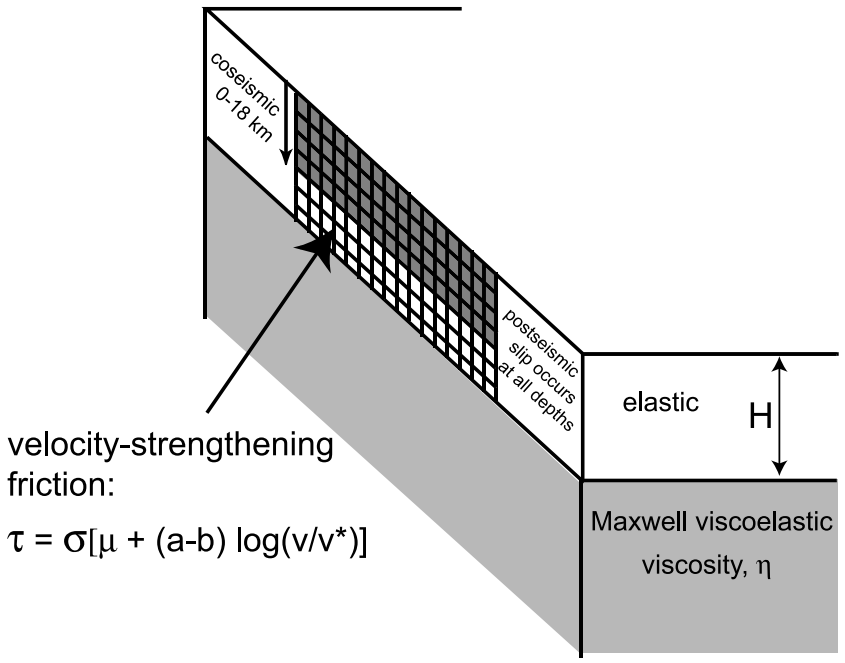

Figure 2. Illustration of model showing discretized fault surface in elastic lithosphere overlying viscoelastic asthenosphere. Coseismic slip is allowed to occur from the surface to 18 km depth. The entire discretized fault surface is allowed to creep following the earthquake. The velocity-strengthening slip law is employed to model afterslip. Uniform frictional properties are assigned to the fault.

*j*th time increment is

$$\tau_i(t_j) \approx \tau_i^c(t_j) + \sum_{k=1}^{j-1} \mathbf{g}_i(t_j - t_k)\mathbf{s}_k, \quad (3)$$

where the $\mathbf{s}_k$ are $m \times 1$ vectors of average slip during the kth time step. We assume that the fault is slipping at steady-state velocity, $\mathbf{v}_0$, before the earthquake. Fletcher (2002) and Matmon *et al.* (2006) estimated a slip rate of 0.008–0.012 m yr^{-1} for the Denali Fault, so we assume $v_0 = 0.01$ m yr^{-1} for depths greater than 18 km and $v_0 = 10^{-4}$ m yr^{-1} (effectively, locked) for depths less than 18 km. Letting v^* in eq. (1) be equal to v_0, such that the initial stress before the earthquake is $\tau_0 = \sigma\mu$, then from eq. (1), the average afterslip rate on the *i*th patch during the *j*th time interval is

$$v_i(t_j) = v_0 \exp\left\{\frac{\tau_i(t_j) - \tau_0}{\sigma(a-b)}\right\}, \quad (4)$$

where $\tau_i(t_j)$ is given by eq. (3). Here, $v > 0$ indicates right-lateral sense of slip. It is clear from eq. (4) that $\tau > \tau_0$ generates slip at a higher rate than v_0 and $\tau < \tau_0$ generates slip at a lower rate than v_0. Eq. (4) does not permit left-lateral slip and therefore areas of the fault that slip coseismically and experience a drop in shear stress will essentially stop sliding following the earthquake. The slip during the *j*th time interval on the *i*th patch is determined by a simple numerical integration, $s_i(t_j) = v_i(t_j)\,\delta_j$, where the duration of the time interval, δ_j, is inversely proportional to $v_i(t_j)$ and is tuned to give sufficient integration accuracy. Let $\mathbf{s}(t_j)$ be the $m \times 1$ vector of average slip on all m patches during the *j*th time increment. Because we have removed a pre-earthquake trend from the GPS time-series data, we compute the slip during the *j*th time interval in excess of the slip that would accumulate at the pre-earthquake slip rate,

$$\mathbf{s}_{\text{post}}(t_j) = \mathbf{s}(t_j) - \mathbf{v}_0\delta_j. \quad (5)$$

We emphasize that although $\mathbf{s}_{\text{post}}$ is strictly postseismic slip that occurs in excess of the pre-earthquake slip rate, $\mathbf{s}_{\text{post}}$ does depend on the interseismic slip rate, $\mathbf{v}_0$ and shear stress, τ_0, through eq. (4).

In this model, the entire fault is assumed to be velocity-strengthening and is assigned uniform value of $\sigma(a-b)$. Any part of the fault that experiences a large coseismic shear stress increase will slip rapidly following the earthquake and regions the slip coseismically will experience a large shear stress decrease and effectively lock up after the earthquake. We therefore conceptualize a fault with velocity-weakening patches that are stuck during the interseismic period and rupture during earthquakes surrounded by velocity-strengthening regions that creep during the interseismic period and exhibit rapid afterslip following earthquakes. However, we do not explicitly model the velocity-weakening patches.

3.2 Inversion method

In this work, we jointly invert coseismic and postseismic GPS data for coseismic slip, friction parameter, $\sigma(a-b)$, elastic thickness, H, and asthenosphere relaxation time, t_R. The observation equation for the coseismic part of the problem relates a vector of coseismic offsets, $\mathbf{d}_{\text{co}}$, to a vector of slip on fault patches, $\mathbf{s}_{\text{co}}$,

$$\mathbf{d}_{\text{co}} = \mathbf{G}\mathbf{s}_{\text{co}} + \epsilon_{\text{co}}, \quad (6)$$

where we relate slip to surface displacements through the kernel matrix, $\mathbf{G}$, which is derived from the solution for a rectangular dislocation in an elastic half-space (Okada 1992). The data errors, ϵ_{co}, are assumed to be Gaussian with covariance matrix, Σ_{co} (this is assumed to be a diagonal matrix). We conduct the traditional slip inversion by minimizing the objective function

$$\Phi_1 = ||\Sigma_{\text{co}}^{-1/2}\mathbf{G}\mathbf{s}_{\text{co}} - \Sigma_{\text{co}}^{-1/2}\mathbf{d}_{\text{co}}||^2 + \gamma^2||\nabla^2\mathbf{s}_{\text{co}}||^2, \quad \mathbf{s}_{\text{co}} \geq 0, \quad (7)$$

where ∇^2 is the discrete Laplacian operator, $||\ ||$ denotes the L-2 norm and $\mathbf{s}_{\text{co}} \geq 0$ indicates that slip is constrained to be right-lateral (positive). This is the standard damped least-squares inversion with positivity constraints for slip, where γ is a so-called smoothing parameter that determines the relative weight placed on fitting the data versus smoothing the coseismic slip distribution (e.g. Du *et al.* 1992).

For the postseismic part of the problem, we assume that the time-series positions of GPS sites relative to pre-earthquake positions, $\mathbf{d}_{\text{post}}(t)$, are related to afterslip on the fault (total accumulated slip minus slip accumulated at the pre-earthquake rate), $\mathbf{s}_{\text{post}}(t)$, coseismic slip, $\mathbf{s}_{\text{co}}$, and surface displacements associated with distortion of the elastic crust coupled to flow in the mantle, $\mathbf{d}_{\text{visco}}(t)$, through the observation equation,

$$\mathbf{d}_{\text{post}}(t) = \mathbf{d}_{\text{offset}} + \mathbf{G}\mathbf{s}_{\text{co}} + \mathbf{d}_{\text{visco}}(t) + \mathbf{G}\mathbf{s}_{\text{post}}(t) + \Psi(\psi_1, \psi_2, \psi_3, \psi_4) + \epsilon_{\text{post}}, \quad (8)$$

where $\mathbf{G}$ is the same kernel matrix as in (6) and $\mathbf{d}_{\text{offset}}$ is a vector of constants that account for unknown pre-earthquake positions for campaign sites or new continuous GPS sites that do not have measurements before the earthquake. The data errors, ϵ_{post}, are assumed to be Gaussian with covariance matrix, Σ_{post} (this is assumed to be a diagonal matrix). Ψ is a vector of sinusoidal terms that model non-tectonic seasonal variations in the time-series positions of continuous GPS sites

$$\Psi(\psi_1, \psi_2, \psi_3, \psi_4) = \psi_1 \sin(2\pi t) + \psi_2 \cos(2\pi t) + \psi_3 \sin(4\pi t) + \psi_4 \cos(4\pi t), \quad (9)$$

where the ψ_i are different for each continuous GPS site and both east and north components. This is a standard approach for accounting for unknown cyclic fluctuations in GPS measurements (e.g. Freed *et al.* 2006a).

Eq. (8) is a highly non-linear relationship between the observables, $\mathbf{d}_{\text{post}}(t)$, and the model parameters because: (1) $\mathbf{s}_{\text{co}}$ depends non-linearly on γ; (2) $\mathbf{s}_{\text{post}}(t)$ depends non-linearly on $\mathbf{s}_{\text{co}}$, $\sigma\mu$, $\sigma(a-b)$, H and t_R and (3) $\mathbf{d}_{\text{visco}}(t)$ depends in turn on $\mathbf{s}_{\text{co}}$ and $\mathbf{s}_{\text{post}}$ as well as non-linearly on H and t_R. We seek values of these parameters, through an inversion, that reproduce the observed GPS time-series. The complete inverse solution would be the joint posterior probability distribution for all of the unknown parameters, which contains all information about the solution including the most likely solution and a description of the model uncertainties. However, it would be computationally burdensome to estimate the posterior probability distributions of the model parameters because a forward model computation of the postseismic displacements (eq. 8) requires computing a non-negative least-squares inversion for coseismic slip, a numerical computation of displacements and stresses at many time intervals using a propagator matrix code, and a numerical computation for the afterslip evolution with time. We take a less exhaustive approach and seek a set of optimal model parameters. The optimal solution is the set of parameters that minimizes the objective function

$$\Phi_2 = \Phi_1 + ||\Sigma_{\text{post}}^{-1/2}(\hat{\mathbf{d}} - \mathbf{d}_{\text{post}})||^2, \quad (10)$$

where $\hat{\mathbf{d}}$ is a vector of predicted postseismic time-series positions and Φ_1 is the objective function defined in (7). In the standard

slip-inversion method, the value for γ in the objective function, Φ_1, must be specified and a separate technique must be introduced to select an optimal value for this parameter (e.g. Fukuda & Johnson 2008). However, following Johnson *et al.* (2006), we have set up this problem so that we simultaneously invert coseismic and postseismic data such that the smoothing parameter, γ, can be optimized with this objective function. The objective function (10) is a function of all the unknown parameters in this problem,

$$\Phi_2 = \Phi_2(\gamma, a\sigma, H, t_{\rm R}, \psi_1, \psi_2, \psi_3, \psi_4). \quad (11)$$

We minimize the objective function, Φ_2, (10) using the following procedure: (1) select a value for γ and invert coseismic GPS displacements for fault slip using the standard, damped least-squares slip-inversion method with positivity constraints to minimize Φ_1; (2) select values for $\sigma\ (a-b)$, H and $t_{\rm R}$, compute the coseismic stress change from the coseismic slip distribution to use as the initial stress condition for the numerical integration of (1) to obtain the evolution of afterslip, $\mathbf{s}_{\rm post}(t)$; (3) compute the predicted surface positions, $\mathbf{Gs}_{\rm post}(t) + \mathbf{d}_{\rm visco}(t)$ and use least squares to invert eq. (8) for the seasonal terms (ψ_1, ψ_2, ψ_3, ψ_4) and offsets ($\mathbf{d}_{\rm offset}$) with $\mathbf{Gs}_{\rm co}$, $\mathbf{d}_{\rm visco}(t)$ and $\mathbf{Gs}_{\rm post}(t)$ fixed and (4) compute the value for the objective function, Φ_2, (10). A minimum value for Φ_2 is found using a simple downhill search method, computing steps 1–4 for each set of model parameters until Φ_2 does not change within a specified tolerance.

To provide an estimate of the uncertainties of the most important posterior model parameters, we approximate the posterior joint marginal distribution of H and $t_{\rm R}$ and marginal posterior distribution of $\sigma(a-b)$. Assuming Gaussian data errors with covariance matrix, Σ_d, the posterior distribution of model parameters given N data and fixed coseismic slip distribution (fixed γ^2) is

$$p(\alpha^2, H, t_{\rm R}, \sigma(a-b)|\mathbf{d}_{\rm post}, \gamma^2) = \frac{1}{(2\pi\alpha^2)^{N/2}} \exp\left[\frac{-1}{2\alpha^2}(\mathbf{d}_{\rm post} - \hat{\mathbf{d}})^T \Sigma_d^{-1}(\mathbf{d}_{\rm post} - \hat{\mathbf{d}})\right], \quad (12)$$

where α^2 is an unknown scalar multiplier of the data variance matrix and will be estimated (e.g. Fukuda & Johnson 2008). It is computationally intensive to estimate the distribution (12), so we instead estimate the distributions $p(\alpha^2, H, t_{\rm R}|\mathbf{d}_{\rm post}, \gamma^2, \hat{\sigma}(a-b))$ and $p(\alpha^2, \sigma(a-b)|\mathbf{d}_{\rm post}, \gamma^2, \hat{H}, \hat{t_{\rm R}})$ with H and $t_{\rm R}$ or $\sigma(a-b)$ fixed to the values determined using the optimization scheme described above (hat symbol denotes optimal value). These distributions are estimated by first computing $\hat{\mathbf{d}}$ at regularly spaced points in H–$t_{\rm R}$ space, or $\sigma(a-b)$ space, and then sampling the distributions using a Monte Carlo-Metropolis algorithm (e.g. Fukuda & Johnson 2008), interpolating at values between the regularly spaced values. We also consider a double-exponential error model for the data, in which the joint posterior probability distribution is

$$p(\alpha, H, t_{\rm R}, \sigma(a-b)|\mathbf{d}_{\rm post}, \gamma^2) = \frac{1}{(2\alpha)^N} \exp\left[\frac{-1}{2\alpha}\sum_{k=1}^{N}|(d^k_{\rm post} - \hat{d}^k)|\right], \quad (13)$$

where $d^k_{\rm post}$ and $\hat{d}^k$ denote the kth measured and predicted time-series position, respectively. The posterior distributions for fixed H and $t_{\rm R}$ or $\sigma(a-b)$ are determined similarly as above for the Gaussian error model.

4 RESULTS

The objective function (10) is minimized with values of $H = 81$ km, $t_{\rm R} = 15$ yr (corresponding to $\eta = 6 \times 10^{18}$ Pa s), and $\sigma\ (a-b) = 0.48$ MPa. The estimates of the posterior probability distributions, using the method described above, are shown in Fig. 3. The double-exponential and Gaussian error models for the data result in very different estimates of elastic thickness and relaxation time, although the 95 per cent confidence regions for both error models are relatively small. The small formal model parameter uncertainties are probably not representative of the true uncertainty in parameters, however. Fig. 4 shows the fit to the data for the best-fitting models for the two data error structures. The model with elastic thickness of 45 km and asthenosphere relaxation time of 50 yr fits the data qualitatively as well as the model with an 81 km thick elastic layer and asthenosphere relaxation time of 15 yr. The formal uncertainties on model parameters as shown in Fig. 3 are probably excessively small because the inversion does not properly take into consideration uncertainty in the earth model and perhaps because of systematic misfit to the data. The estimated elastic layer thickness of about 45–85 is similar to or larger than the average crustal thickness of 50 km in central Alaska (Brocher *et al.* 2004) suggesting that viscous flow dominantly occurs in the upper mantle and not in the lower crust.

The coseismic slip and cumulative afterslip distributions are shown in Figs 5(a) and (b) for $H = 45$ km and $t_{\rm R} = 50$ yr. The magnitude of right-lateral slip is shown on each patch. The coseismic slip is concentrated in five patches, similar to that inferred by others

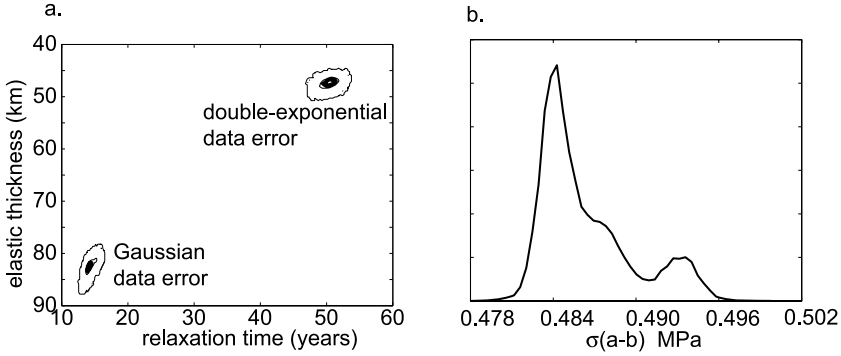

Figure 3. (a) Contours of posterior probability for Gaussian and double-exponential data error models. Outer contour corresponds approximately with the boundary of the 99 per cent confidence region. Joint distribution of relaxation time and elastic thickness assuming optimized values (Gaussian data error model) for $\sigma(a-b)$ and smoothing parameter, γ^2. (b) Marginal posterior probability distribution for $\sigma(a-b)$ assuming optimized values (Gaussian data error model) for elastic thickness and relaxation time.

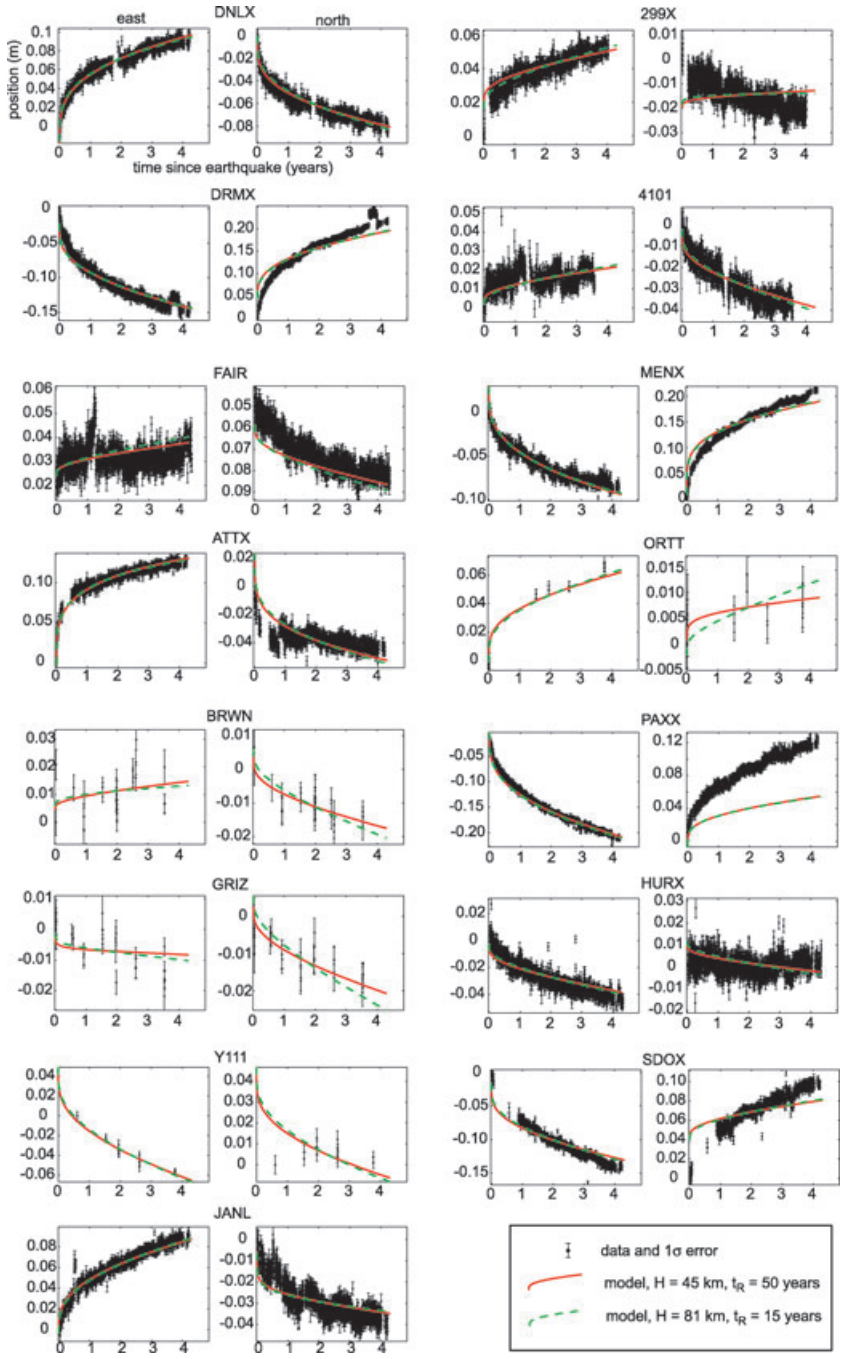

Figure 4. GPS time-series and 1σ errors. A pre-earthquake linear trend has been removed from the data. Axes labels are shown only for the first plot and are the same for all plots (vertical axis is position in metres and horizontal axis is time since the earthquake in years). For each pair of plots, the east component of position is shown on the left-hand side and the north component of position on the right-hand side. Red, solid curves show best-fitting model for the case of Gaussian data errors. Dashed, green curves show best-fitting model for the case of double-exponential data errors. Periodic seasonal variations in the time-series are estimated in the inversions but are not shown in the plots.

(e.g. Wright *et al.* 2004; Hreinsdóttir *et al.* 2006; Elliot *et al.* 2007). Most of the afterslip is concentrated between 18 and 30 km depth below the three largest coseismic slip patches. Smaller amounts of afterslip occur at shallower depths between the coseismic slip patches. The inferred patches of afterslip above 18 km depth is similar to that imaged in a kinematic slip inversion in Freed *et al.* (2006a) which shows a patch of afterslip consistent with the patch at a distance of about 200 km from the west end of the fault in Fig. 5(b). The time evolution of afterslip on three patches is shown in Fig. 5(c). The slip on patch 2 (patch with maximum cumulative afterslip) exhibits the most rapid afterslip in the first days following the earthquake, while the shallowest patch (patch 1) exhibits much lower slip rates during this time and afterslip on the deepest patch (patch 3) actually accelerates slowly for the first 3 months before decelerating. After about half a year following the earthquake, the afterslip decelerates at similar rates on all three patches. After 4.5 yr, the slip rate over much of the fault below 18 km depth is about 0.009 m yr^{-1} faster than the pre-earthquake rate of 0.01 m yr^{-1}.

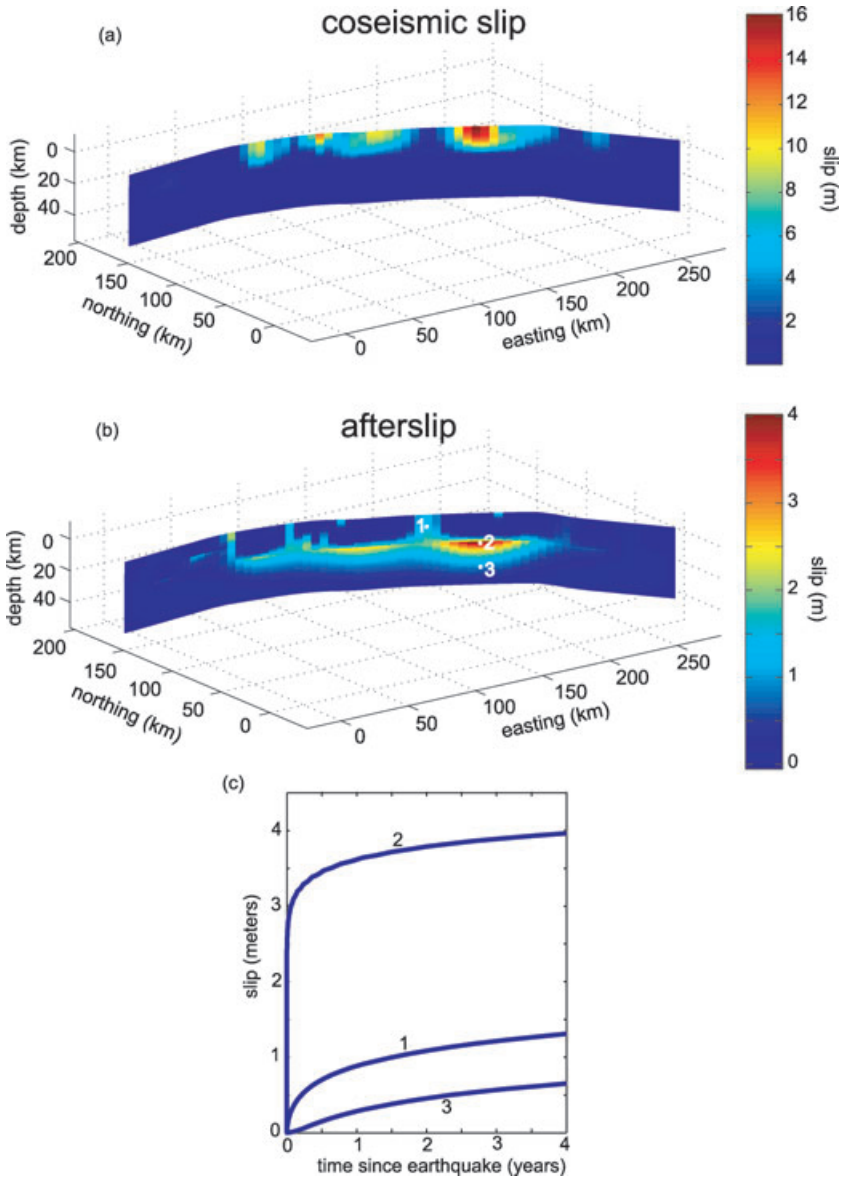

Figure 5. Slip distributions for optimal solution determined assuming double-exponential data errors ($H = 45$ km, $t_R = 50$ yr, σ(a − b) = 0.5 MPa). (a) Coseismic slip distribution showing magnitude of right-lateral slip. Coseismic slip is constrained to depths of 0–18 km in the inversion although fault is shown to extend to depth of 45 km. (b) 4-yr cumulative afterslip showing magnitude of right-lateral slip. Afterslip extends to the bottom of the elastic plate (bottom of shown fault surface) and is concentrated immediately below and between large coseismic slip patches. (c) Slip evolution with time on three patches labelled in (b).

The fit to the time-series is shown in Fig. 4 without the sinusoidal seasonal terms. The fit is generally better in the east component than the north component. Most of the east component time-series positions are fit within the uncertainties. There is a systematic misfit in the north component that we discuss below. The observed high surface velocities in the first few months after the earthquake and the lower velocities at later times are reproduced well at both near-fault sites (e.g. DNLX) and sites far from the fault (e.g. FAIR). However, the rapid postseismic signal in the first few months is underpredicted at a few of the sites located 100–300 km from the fault (e.g. sites 299X and 4101) suggesting a possible missing postseismic source in our model such as afterslip deeper on the fault or distributed, non-linear viscous flow at depth (Freed *et al.* 2006b).

Fig. 6 shows the observed and computed cumulative 4-yr postseismic displacements. Most of the displacements on the northern side of the Denali Fault are fit within the 2σ error ellipses, but there are significant misfits on the southern side of the fault. As mentioned above, the misfit is especially large in the north component of the displacements such as seen at sites clustered near latitude 62°N. Significant misfits near the Totschunda segment (between 142° and 144°W and 62° and 63°N) may be due to mismodelled shallow afterslip. It is important to note that although it is illustrative to look at the residuals in Fig. 6, we did not minimize the misfit between observed and computed cumulative displacements, rather, we modelled the time-series positions.

We did not invert the vertical component of GPS data because the vertical time-series are relatively noisy and there are systematic misfits between the vertical displacements and postseismic models (e.g. Freed *et al.* 2006a, fig. 17), suggesting that hydrologic, ice-unloading, or other processes not considered in our study

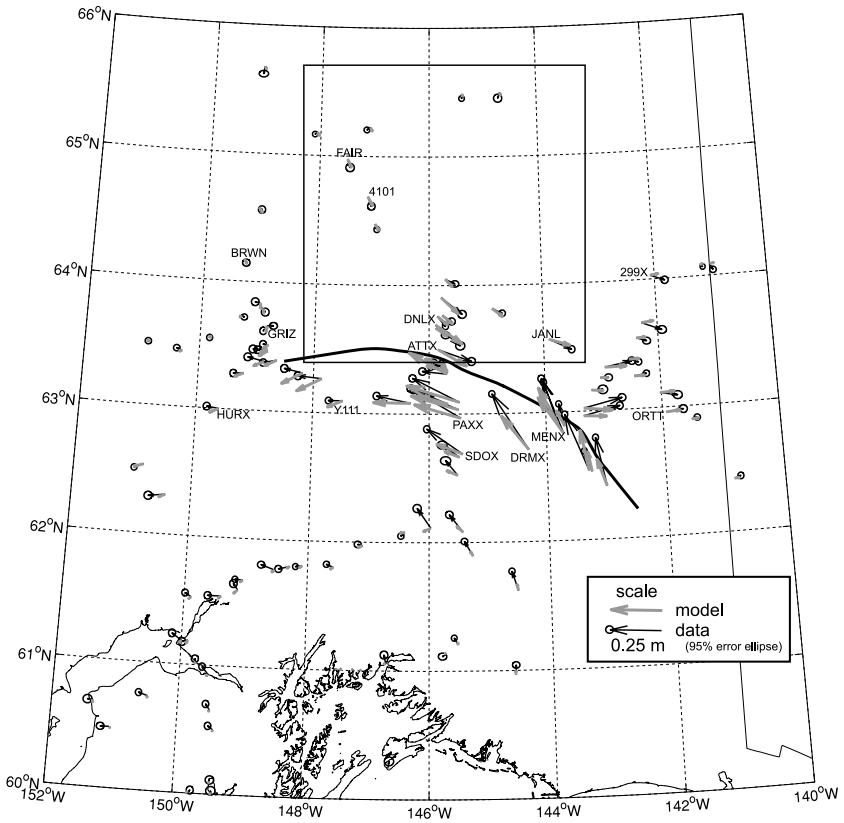

Figure 6. Observed and predicted cumulative 4-yr postseismic displacements. Time-series for labelled sites are shown in Fig. 4. Box north of fault outlines sites used for profile in Fig. 9.

may contribute to the vertical motions. We show a smoothed, contoured version of the measured cumulative vertical displacements in Fig. 7(a) along with model predictions of the vertical displacements. The displacements in Fig. 7 are relative to site WHIT which is located in western Canada (just east of the figure). Fig. 7(b) shows the predicted vertical displacements for the optimized coupled afterslip/flow model. Fig. 7(c) combines the optimized predicted vertical displacements with the predicted vertical displacements in a fully drained poroelastic half-space (assuming $\nu = 0.29$ and 0.25 for undrained and drained Poisson's ratio, respectively). Although the correspondence between the smoothed vertical displacement field in Fig. 7(a) and the prediction in Fig. 7(c) is not exact, the patterns are similar with a four-quadrant distribution of uplifted and subsided regions.

Fig. 8 shows the fit to the data for $H = 45$ km and $t_R = 50$ yr with and without the contribution to surface displacements from viscous flow in the asthenosphere. The predicted time-series for the case without the contribution from viscous flow is simply computed by setting the term $\mathbf{d}_{\text{visco}}(t)$ in eq. (8) equal to zero. The comparison illustrates the relative contributions to surface displacement from mantle flow and afterslip. The contribution to surface displacement from deep viscous flow is insignificant at sites near the fault (e.g. ATTX, Fig. 6) and small but significant at sites far from the fault (e.g. FAIR and 4101, Fig. 6).

Fig. 9 shows the fit to the data for the case $H = 45$ km and $t_R = 50$ yr and for a the best-fitting model with afterslip only (no viscous flow in the asthenosphere). The afterslip-only inversion was conducted by minimizing the objective function (10) using eq. (8) without the term $\mathbf{d}_{\text{visco}}(t)$. The fit is nearly identical for the two models at the two sites nearest the fault (DNLX and JANL) and slightly different at the farthest sites (FAIR and 4101). Fig. 9 also plots the cumulative, 4 yr displacements at sites located in the box north of the fault shown in Fig. 6. Both models systematically underpredict cumulative displacements and the afterslip-only model underpredicts displacements slightly worse than the coupled afterslip/flow model.

5 DISCUSSION

For typical laboratory values of $a - b$ of order 10^{-2} at temperatures corresponding to depths greater than 18 km (e.g. Blanpied *et al.* 1995), our estimate of $\sigma(a - b) = 0.48$ implies effective normal stress of about 50 MPa which is lower than effective normal stress of 360–800 MPa under hydrostatic pore pressures between 18 and 40 km depth. Therefore, either the value of $a - b$ for the Denali Fault is about an order of magnitude lower than laboratory values or elevated pore pressure in the fault zone reduces $\sigma(a - b)$. This value of $\sigma\ (a - b)$ is comparable to values obtained using similar models of afterslip for other earthquakes. Hearn *et al.* (2002) estimated a value of 0.2–0.4 MPa using postseismic data from the 1999 Izmit, Turkey earthquake and Perfettini & Avouac (2007a) estimated a value of 0.5 MPa using postseismic data from the 1992 Landers, California earthquake. Several other studies also infer values of $\sigma(a - b)$ in the range 0.2–0.7 MPa from postseismic geodetic data (Miyazaki *et al.* 2004; Hsu & Bock 2006; Perfettini & Avouac 2007b). Consistent with our estimate of small σ, Wesson & Boyd (2007) infer low absolute shear stress (1–4 MPa) at a depth of about 5 km in the vicinity of the Denali Fault using stress tensor inversion of focal mechanisms before and after the Denali Fault earthquake.

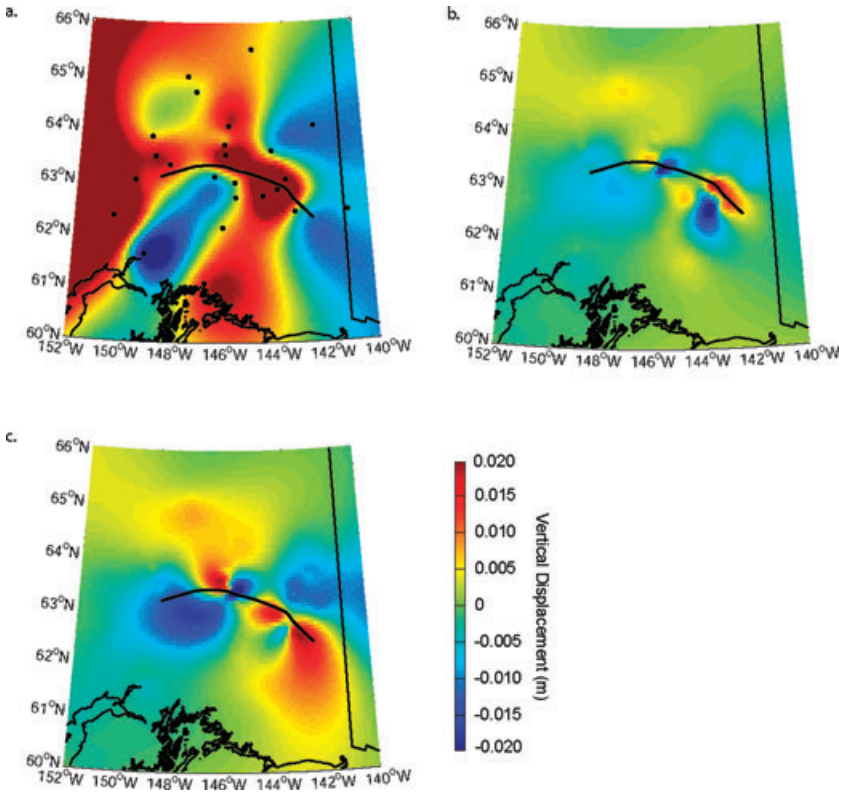

Figure 7. (a) Contoured 4-yr cumulative vertical displacements measured with GPS. Displacements are relative to site WHIT which is located in western Canada. Contour algorithm forces the surface to go through data (block dots) and interpolates between points with splines. (b) Modelled vertical displacements assuming $H = 45$ km and $t_R = 50$ yr. (c) Same as (b) but with additional vertical displacement predicted by a model for a fully drained poroelastic half-space. The observed gross uplift/subsidence pattern is similar to the predicted pattern and the magnitude of uplift/subsidence is better predicted in (c) with the additional contribution from poroelasticity.

Assuming a coefficient of friction of 0.6, the 1–4 MPa shear stress is consistent with an effective normal stress on the fault at 5 km depth of less than 10 per cent of the lithostatic load minus hydrostatic pore pressure, similar to our independent estimate.

There is much discussion in the literature regarding the nature of deformation in the lower crust. For example, there is evidence that the lower crust deforms as a broad zone of distributed shear and other evidence that deformation in the crust is largely confined to narrow shear zones that are the ductile downward extension of brittle faults in the upper crust (e.g. Bürgmann & Dresen 2008). Unfortunately, it is not yet possible to distinguish between these two possibilities for the Alaskan crust using only postseismic data from the Denali Fault earthquake. Our results demonstrate that horizontal postseismic GPS time-series data are consistent with models in which lower crustal deformation is confined to afterslip on a discrete fault or narrow shear zone. However, Freed *et al.* (2006b) demonstrate that these data are also consistent with models of distributed flow in the lower crust without afterslip on a discrete, through-going fault in the lower crust. This ambiguity has arisen in models of postseismic deformation following other large earthquakes. For example, postseismic deformation of the lower crust following the Landers, California earthquake has been attributed to afterslip (e.g. Savage & Svarc 1997; Fialko 2004) and distributed viscous flow (e.g. Deng *et al.* 1998).

Our inversions attribute most of the postseismic signal to afterslip on the fault. However, models with non-linear (Freed *et al.* 2006b) or biviscous (Pollitz 2005) asthenosphere viscosity can reproduce time-series observations at far-field sites. Presumably a coupled afterslip/viscous flow model that incorporates non-linear or biviscous asthenosphere flow could reproduce the data with a larger contribution from viscous flow. The plot of cumulative displacements with distance from the fault in Fig. 9 shows that both the coupled afterslip/viscous flow model and the afterslip-only model systematically underpredict displacements. The afterslip-only model underpredicts cumulative displacements slightly worse than the coupled model indicating that the additional contribution of asthenosphere flow to surface displacements improves the fit some. The systematic underprediction of displacements might be reconciled with a contribution to surface displacements from flow in the asthenosphere of a material with an effective viscosity that varies with time.

Although the general patterns observed in the time-series and cumulative displacements are reproduced well in a qualitative sense by this fairly simple model of postseismic deformation, there is a systematic, asymmetric pattern of misfit shown in Fig. 10 between the measured 4-yr cumulative postseismic displacements and the model. On the north side of the Denali Fault, the residual vectors are mostly within the 2 σ uncertainty ellipses and nearly randomly oriented. But on the south side of the Denali Fault, the residual displacements are systematically oriented to the northwest, similarly to the plate convergence direction (Fig. 1). As our data set has been corrected for interseismic deformation based in large part on GPS rates determined at these sites during the years prior to the earthquake, this cannot be attributed to background elastic plate boundary strain.

We consider the possibility that lateral variations in crustal/lithosphere rheology could account for the observed

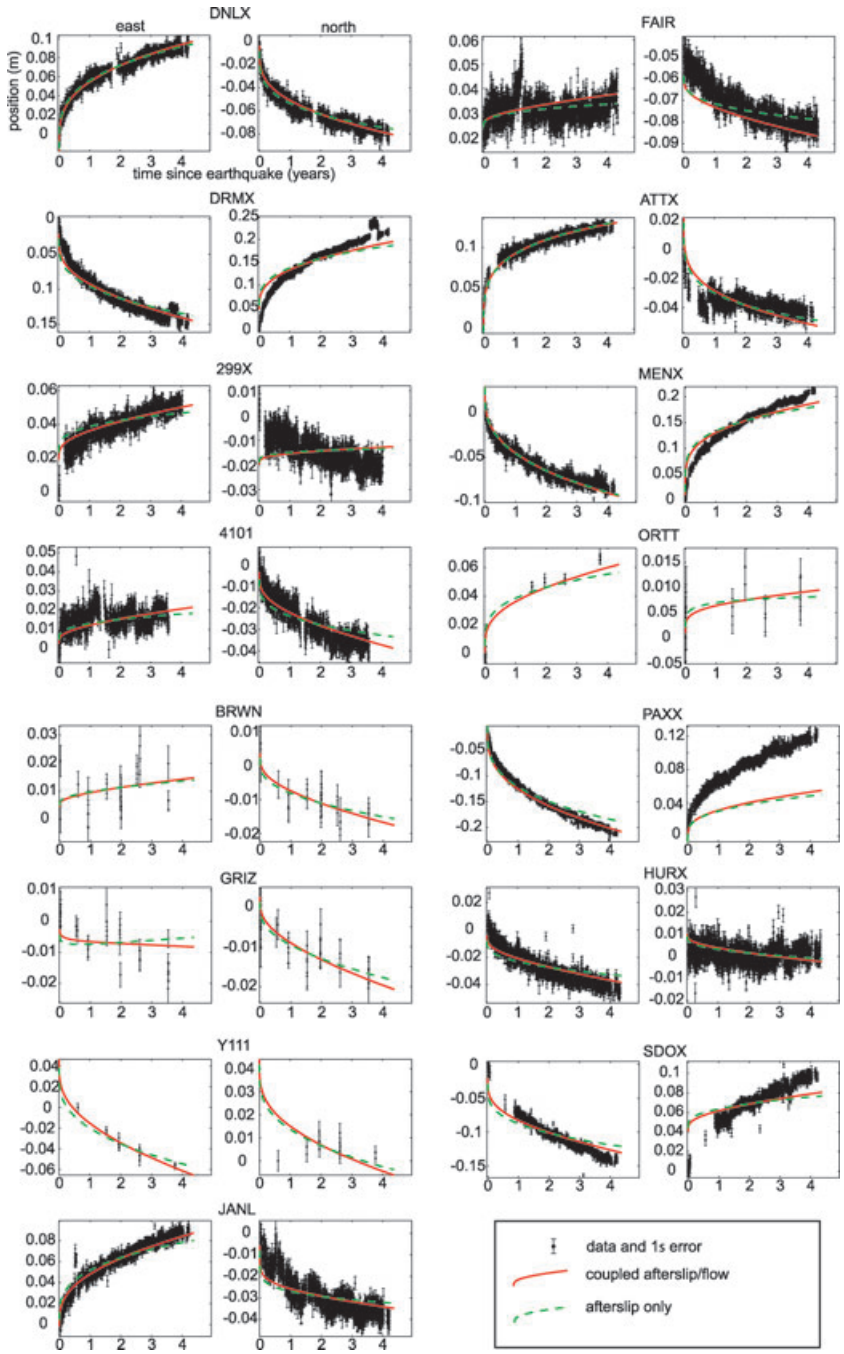

Figure 8. GPS time-series and 1σ errors. A pre-earthquake linear trend has been removed from the data. Axes labels are shown only for the first plot and are the same for all plots (vertical axis is position in metres and horizontal axis is time since the earthquake in years). For each pair of plots, the east component of position is shown on the left-hand side and the north component of position on the right-hand side. Plot compares model prediction with and without the contribution to surface displacements from viscous flow in the asthenosphere. Red, solid curves show best-fitting coupled afterslip/viscous flow model for the case of Gaussian data errors. Dashed, green curves show predictions from the same model, but without the contribution to surface displacements from viscous flow. Periodic seasonal variations in the time-series are estimated in the inversions but are not shown in the plots.

asymmetric pattern in surface displacements. The subducting slab beneath southern Alaska is one obvious source of lateral variation in lithosphere structure (e.g. Eberhart-Phillips *et al.* 2006). Also, tomographic inversions by Eberhart-Phillips *et al.* (2006) indicate that the crust is thicker on the southern side of the Denali Fault than the northern side. We constructed simplified 2-D models of a strike–slip fault that crudely incorporate these lateral variations using a boundary element technique. We extend the popular displacement-discontinuity boundary element method for elasticity (e.g. Crouch & Starfield 1983) to incorporate linear Maxwell viscoelastic domains. Figs 11(a) and (b) show the assumed geometry for the two cases and Fig. 11(c) shows the velocity profiles across the fault. In the model, we impose 6 m of sudden slip on the locked portion of the fault and allow the viscoelastic substrate below to

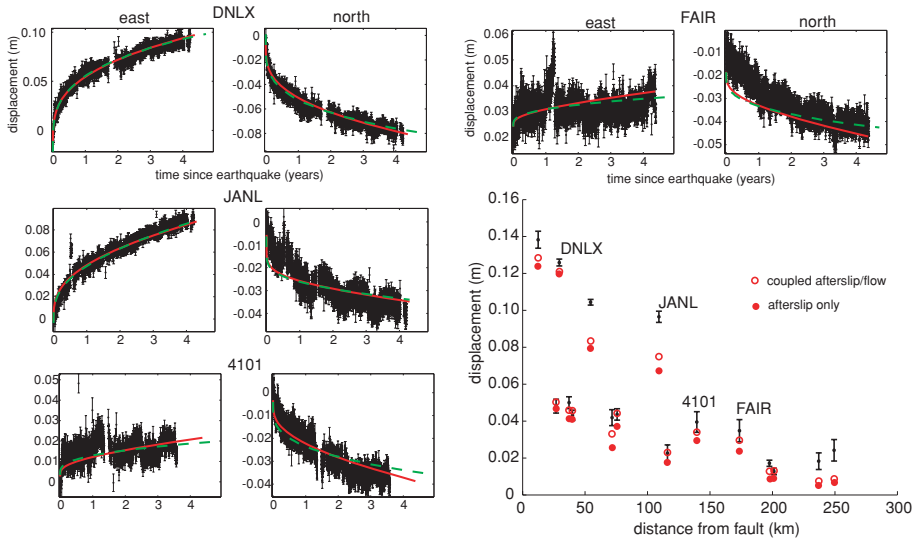

Figure 9. GPS time-series and 1σ errors for selected sites within the box in Fig. 6. Red, solid curves show best-fitting coupled afterslip/viscous flow model for the case of Gaussian data errors. Dashed, green curves show best-fitting model assuming no asthenosphere flow (afterslip only) for the case of Gaussian data errors. Also shown is plot of observed and predicted cumulative 4 yr displacements at sites within the box in Fig. 6. Both models systematically underpredict the cumulative displacements.

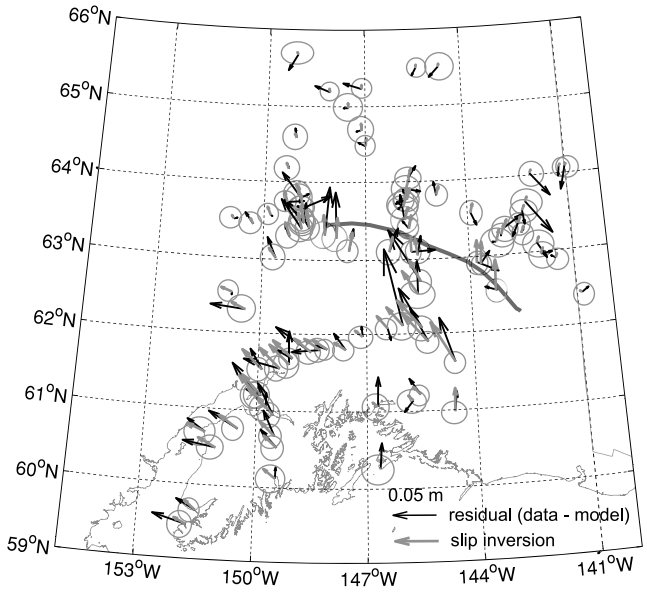

Figure 10. Black vectors are residual cumulative 4-yr displacement vectors (observed—model) centred on the 95 per cent data uncertainty ellipses. Model is the case $H = 45$ km and $t_R = 50$ yr. Note the systematic misfit pattern to the south of the fault, with residual vectors pointing to the NW, suggesting a missing source of deformation. Residual vectors north of the fault are largely within the error ellipses and randomly oriented suggesting the model satisfactorily accounts for this part of the signal. Heavy grey arrows show predicted surface displacements for the slip inversion shown in Fig. 11.

flow in response to the sudden load. The plots show the surface velocities 4 yr after the imposed earthquake. The asymmetry in the model surface displacements is opposite to the observed asymmetry in surface displacements. The models display higher velocities on the north side of the fault, whereas the displacements (velocities) are observed to have been larger on the south side of the fault. Therefore, a contrast in effective elastic thickness across the fault cannot account for the observed asymmetry in the displacement residuals.

The residual displacement field actually resembles the interseismic velocity field in this region (e.g. Ohta *et al.* 2006) due to locking of the plate interface and accumulating elastic strain in the overriding plate. Therefore, we consider the possibility that the residuals are due to transiently increased coupling of the plate interface. We model interface coupling with backslip of elastic dislocations in an elastic half-space following the now-standard approach introduced by Savage (1983). We invert for the distribution of backslip using the same slip-inversion scheme adopted for the coseismic slip inversion described previously. The smoothing parameter is selected subjectively to give a qualitatively smooth backslip distribution. The backslip is shown in Fig. 11(d) and the fit to the residual displacements is shown in Fig. 10. The fully locked region of the plate interface inferred by Ohta *et al.* (2006) is shown in Fig. 11(d). Ohta *et al.* (2006) infer the region immediately surrounding this fully locked patch to be partly locked (non-zero sliding but at a rate lower than plate convergence). The general residual displacement pattern is reproduced by backslip on the interface in the areas surrounding the fully locked patch. This result hints at the possibility that some of the increased velocities south of the Denali Fault following the earthquake could be due to decreased creep rate of the plate interface below the locked section, but it is difficult to identify a mechanism for such widespread reduction in creep rate. Further more, the imaged backslip rate on the far right-hand side (Yakutat Slab, Fig. 1) is considerably higher than the plate convergence rate. The effect of the Denali Fault earthquake is to increase the downdip component of shear stress on the subduction interface near 144°W, 61°N, which would promote decreased creep rate at the interface. The maximum shear stress change in this region is about 50 kPa, which according to spring-slider calculations with rate-state friction (e.g. Johnson *et al.* 2006), is sufficient to cause the interface to locally lock up for several years for a narrow range of friction parameters. However, the shear stress changes over most of the interface are too small to generate appreciable widespread reduction in creep rate.

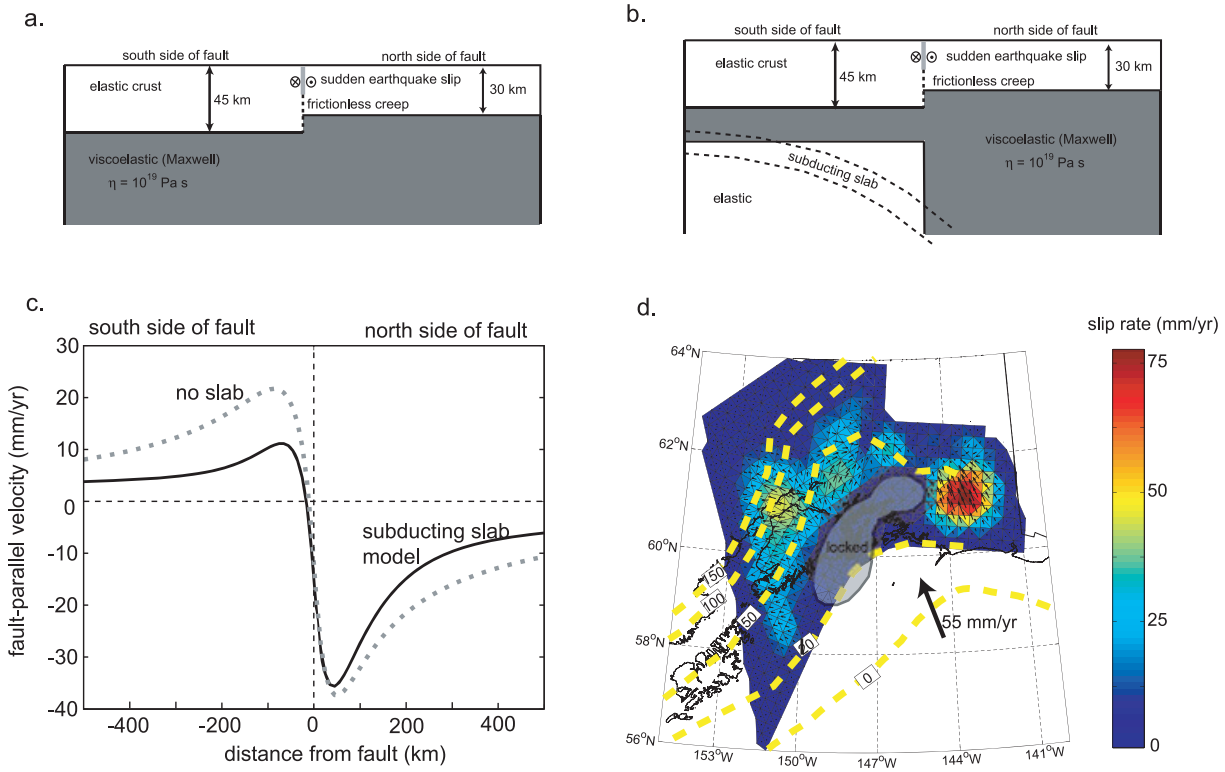

Figure 11. (a) Illustration of geometry of 2-D boundary element model of a vertical strike–slip fault in elastic lithosphere with variable thickness overlying a viscoelastic asthenosphere. (b) Illustration of 2-D boundary element model of simplified geometry of a strike–slip fault in an elastic lithosphere with variable thickness overlying an elastic subducting slab in a viscoelastic asthenosphere. (c) Velocity profiles for 2-D models in (a) and (b) after a sudden displacement discontinuity of 6 m is imposed on the fault. Note that the asymmetry in the predicted velocity profiles is opposite to the observed asymmetry in the residual displacement pattern in Fig. 10. (d) Inversion for backslip on subducting plate interface. The backslip might represent reduced forward slip on the subduction interface following the earthquake. The geometry and location of the locked asperity is from Ohta *et al.* (2006). Backslip is assumed to be zero within the asperity.

6 CONCLUSIONS

We model coseismic GPS displacements and 4 yr of postseismic GPS time-series positions with a coupled model of afterslip on the fault in the lithosphere and distributed viscous flow in the asthenosphere. Afterslip is assumed to be governed by a laboratory-derived rate-strengthening friction law. The postseismic GPS time-series are best reproduced with a 45–85-km-thick elastic lithosphere overlying asthenosphere with viscosity of 0.6–1.5 $\times$ 10^{19} Pa s. The inferred 45–85 km lithosphere thickness is equal to or larger than the crustal thickness in the region inferred from seismology suggesting that deformation in the lower crust is confined largely to slip on a discrete fault penetrating the entire crust with distributed viscous flow occurring largely below the crust in the upper mantle. However, this is not a unique result as previous studies using a shorter time span of data have shown that the postseismic GPS data can also be explained with distributed flow in the lower crust. For our best-fitting value of $\sigma(a - b) = 0.48$ MPa and typical laboratory values of $a - b$ of order 10^{-2}, the effective normal stress on the fault is 50 MPa, which is about an order of magnitude lower than lithostatic confining pressure minus hydrostatic pore pressure. We find that at least two mechanisms, afterslip at crustal depths on the fault and distributed viscous flow in the mantle, are probably necessary to reproduce the postseismic time-series data at sites located more than 100 km from the fault, although our inversions attribute most of the postseismic deformation to afterslip on the fault. Models that do not incorporate mantle flow (afterslip only) underpredict the far-field displacements while models that include mantle flow improve the fit but still systematically underpredict cumulative surface displacements. It is clear from several previous studies that the postseismic GPS time-series cannot be reproduced with models incorporating strictly Newtonian viscosity for the mantle and/or a crustal shear zone. Previous studies showed that models that incorporate either non-linear power-law mantle flow or linear biviscous mantle flow can reproduce the GPS time-series at sites far enough from the fault that are not highly influenced by shallow afterslip. Our results show that it is possible that the non-Newtonian behaviour that is inferred from the GPS time-series may occur at crustal depths as afterslip within a shear zone with velocity-strengthening friction.

ACKNOWLEDGMENTS

The authors are grateful to the associate editor, Jim Savage, and Hugo Perfettini for thoughtful reviews. The work was supported by NSF grant EAR-0309946.

REFERENCES

Blanpied, M.L., Lockner, D.A. & Byerlee, J.D., 1995. Frictional slip of granite at hydrothermal conditions, *J. geophys. Res.*, **100**(B7), 13 045–13 064.

Brocher, T., Fuis, G., Lutter, W., Christensen, N. & Ratchkovski, N., 2004. Seismic velocity models for the denali fault zone along the richardson highway, alaska, *Bull. seism. Soc. Am.*, **94**(6B), S85–S106.

Bürgmann, R. & Dresen, G., 2008. Rheology of the lower crust and upper mantle: Evidence from rock mechanics, geodesy and field observations, *Rev. Earth Plan. Sci.*, **36**, doi:10.1146/annurev.earth.36.031207.124326, 531–567.

Crouch, S.L. & Starfield, A.M., 1983. *Boundary Element Methods in Solid Mechanics,* Allen & Unwin Inc., Winchester, MA.

Deng, J., Gurnis, M., Kanamori, H. & Hauksson, E., 1998. Viscoelastic flow in the lower crust after the 1992 landers, california earthquake, *Science*, **282**, 1689–1692.

Dieterich, J.H., 1981. Constitutive properties of faults with simulated gouge, in *Mechanical Behavior of Crustal Rocks (Geophys. Monogr. Ser.)*,Vol. 24, pp. 103–120, ed. Carter, N.L. *et al.*, American Geophysical Union, Washington, DC.

Du, Y., Aydin, A. & Segall, P., 1992. Comparison of various inversion techniques as applied to the determination of a geophysical deformation model for the 1983 borah peak earthquake, *Bull. seism. Soc. Am.*, **82**, 1840–1866.

Eberhart-Phillips, D., Christensen, D. & Brocher, T., 2006. Imaging the transition from aluetian subduction to yakutat collision in central alaska, with local earthquakes and active source data, *J. geophys. Res.*, **111**(B11303), doi:10.1029/2005JB004240.

Elliot, J., Freymueller, J.T. & Rabus, B., 2007. Coseismic deformation of the 2002 denali fault earthquake: contributions from sar range offsets, *J. geophys. Res.*, **112**(B06421), doi:10.1029/2006JB004428.

Fialko, Y., 2004. Evidence of fluid-filled upper crust from observations of post-seismic deformation due to the 1992 mw7.3 landers earthquake, *J. geophys. Res.*, **109**(B08401), doi:10.1029/2003JB002985.

Fletcher, H.J., 2002. Crustal deformation in alaska measured using the global positioning system, Technical report, *PhD thesis*, University of Alaska Fairbanks, Fairbanks.

Freed, A., Bürgmann, R., Calais, E., Freymueller, J. & Hreinsdóttir, S., 2006a. Implications fo deformation following the 2002 denali, alaska, earthquake for postseismic relaxation processes and lithospheric rheology, *J. geophys. Res.*, **111**(B01401), doi:10.1029/2005JB003894.

Freed, A., Bürgmann, R., Calais, E. & Freymueller, J., 2006b. Stress-dependent power-law flow in the upper mantle following the 2002 denali, alaska, earthquake, *Earth planet. Sci. Lett.*, **252**, 481–489.

Freymueller, J.T., Cohen, S.C., Cross, R., Elliott, J., Fletcher, H.J., Larsen, C., Hreinsdóttir, S. & Zweck, C., 2008. Active deformation processes in alaska, based on 15 years of gps measurements, in *AGU Geophysical Monograph*. eds Freymueller, J.T., Haeussler, P.J., Wesson, R.W. & Ekström, G., American Geophysical Union, **179**, 350 pp.

Fukahata, Y. & Matsu'ura, M., 2006. Quasi-static internal deformation due to a dislocation source in a multilayered elastic/viscoelastic half-space and an equivalence theorem, *Geophys. J. Int.*, **166**, 418–434.

Fukuda, J. & Johnson, K.M., 2008. A fully bayesian inversion for spatial distribution of fault slip with objective smoothing, *Bull. seismol. Soc. Am.*, **98**, doi:10.1785/0120070194.

Hearn, E., Burgmann, R. & Reilinger, R., 2002. Dynamics of izmit earthquake postseismic deformation and loading of the duzce earthquake hypocenter, *Bull. seis. Soc. Am.*, **92**(1), 172–193.

Hreinsdóttir, S., Freymueller, J., Bürgmann, R. & Mitchell, J., 2006. Coseismic deformation of the 2002 denali fault earthquake: insights from gps measurements, *J. geophys. Res.*, **111**(B03308), doi:10.1029/2005JB003676.

Hsu, Y.-J. *et al.* 2006. Frictional afterslip following the 2005 nias-simeulue earthquake, sumatra, *Science*, **312**, doi:10.1126/science.1126960.

Johnson, K., Bürgmann, R. & Larson, K., 2006. Frictional properties on the san andreas fault near parkfield, california, inferred from models of afterslip following the 2004 earthquake., *Bull. seismol. Soc. Am.*, **96**(4B), doi:10.1785/0120050808.

Linker, M. & Rice, J., 1997. Models of postseismic deformation and stress transfer associated with the loma prieta earthquake, in *U.S. Geological Survey Paper 1550-D: The Loma Prieta, California Earthquake of October 17, 1989: Aftershocks and Postseismic Effects*, pp. D253–D275, US Government Printing Office, Washington, DC.

Marone, C., Scholtz, C. & Bilham, R., 1991. On the mechanics of earthquake afterslip, *J. geophys. Res.*, **96**(B5), 8441–8452.

Matmon, A., Schwartz, D., Haeussler, P., Finkel, R., Lienkaemper, J., Stenner, H. & Dawson, T., 2006. Denali fault slip rates and holocene-late pleistocene kinematics of central alaska, *Geology*, **34**(8), 645–648.

Miyazaki, S., Segall, P., Fukuda, J. & Kato, T., 2004. Space time distribution of afterslip following the 2003 tokachi-oki earthquake: implications for variations in fault zone frictional properties, *Geophys. Res. Lett.*, **31**(L06623), doi:10.1029/2003GL019410.

Ohta, Y., Freymueller, J., Hreinsdóttir, S. & Suito, H., 2006. A large slow slip event and the depth of the seismogenic zone in the south central alaska subduction zone, *Earth planet. Sci. Lett.*, **247**, 108–116.

Okada, Y., 1992. Internal deformation due to shear and tensile faults in a half-space., *Bull. seism. Soc. Am.*, **82**, 1018–1040.

Perfettini, H. & Avouac, J.-P., 2007a. Modeling afterslip and aftershocks following the 1992 landers earthquake, *J. geophys. Res.*, **112**(B07409), doi:10.1029/2006JB004399.

Perfettini, H. & Avouac, J.-P., 2007b. Postseismic relaxation driven by brittle creep: a possible mechanism to reconcile geodetic measurements and the decay rate of aftershocks, application to the chi-chi earthquake, taiwan, *J. geophys. Res.*, **109**(B02304), doi:10.1029/2003JB002488.

Pollitz, F.F., 2005. Transient rheology of the upper mantle beneath central alaska inferred from the crustal velocity field following the 2002 denali earthquake, *J. geophys. Res.*, **110**(B08407), doi:10.1029/2005JB003672.

Savage, J., 1983. A dislocation model of strain accumulation and release at a subduction zone, *J. geophys. Res.*, **88**, 4984–4996.

Savage, J. & Svarc, J., 1997. Postseismic deformation associated with the 1992 m=7.3 landers earthquake, southern california, *J. geophys. Res.*, **102**(B7), 7565–7577.

Wesson, R.L. & Boyd, O.S., 2007. Stress before and after the 2002 denali fault earthquake, *Geophys. Res. Lett.*, **34**(L07303), doi:10.1029/2007GL029189.

Wright, T., Lu, Z. & Wicks, C., 2004. Constraining the slip distribution and fault geometry of the mw 7.9, 3 november 2002, denali fault earthquake with interferometric synthetic aperture radar and global positioning system data, *Bull. seism. Soc. Am.*, **94**(6B), S175–S189.